Simultaneous Holographic Imaging of Neuronal Circuits in Three Dimensions

Sean Quirin, PhD, Jesse Jackson, PhD,
Darcy S. Peterka, PhD, and Rafael Yuste, MD, PhD

Department of Biological Sciences
Columbia University
New York, New York

Introduction

In this chapter, we introduce a scanless optical method for simultaneously imaging neuronal activity in three dimensions (3D). Using a spatial light modulator and a custom-designed phase mask, we collect light simultaneously (as opposed to serially) from different focal planes and perform holographic calcium imaging of neuronal activity *in vitro* and *in vivo*. This method could be used as a technological platform for brain activity mapping.

Optical imaging of neural activity has several advantages over alternative strategies for monitoring neurons, such as patch electrodes and electrode arrays. First, it is minimally invasive and allows for the monitoring of large ensembles of neurons with single-cell resolution (Yuste and Katz, 1991). Also, it is compatible with a large variety of functional and chemical sensors (e.g., voltage indicators, calcium indicator, metabolic sensors), with genetically encoded indicators, and thus can be used for chronic imaging of genetically defined cell populations (Chen et al., 2013).

However, several key weaknesses remain for functional imaging of neuronal cell activity. First, from the very first microscope designed by A. van Leeuwenhoek, image acquisition has been limited typically to a single plane, whereas nearly all interesting biological structures are 3D, requiring sequential scanning for volumetric imaging. Second, as a result of this sequential scanning, the sampling rate over the volume data is slow (normally a few Hz) relative to neuronal activity (1 kHz). Moreover, in highly scattering tissue, although two-photon excitation has afforded single-cell resolution and imaging below superficial layers (Horton et al., 2013), images are normally generated by serially scanning a single beam. More recent attempts have been made to circumvent this limitation (Gobel et al., 2007; Nikolenko et al., 2008; Cheng et al., 2011; Katona et al., 2012), but despite recent advances that increase the image acquisition speed, few proposed strategies are scalable toward meeting the challenge of fast, population voltage imaging with single-cell resolution in scattering tissue in 3D. Such a task would require milliseconds of temporal resolution across wide spatial areas (Alivisatos et al., 2012; Kralj et al., 2012).

Volume Projection Imaging

As one solution to this problem, we propose here a scanless structured illumination microscope coupled to a custom imaging system with wavefront coding. This coded imaging system creates a projection of

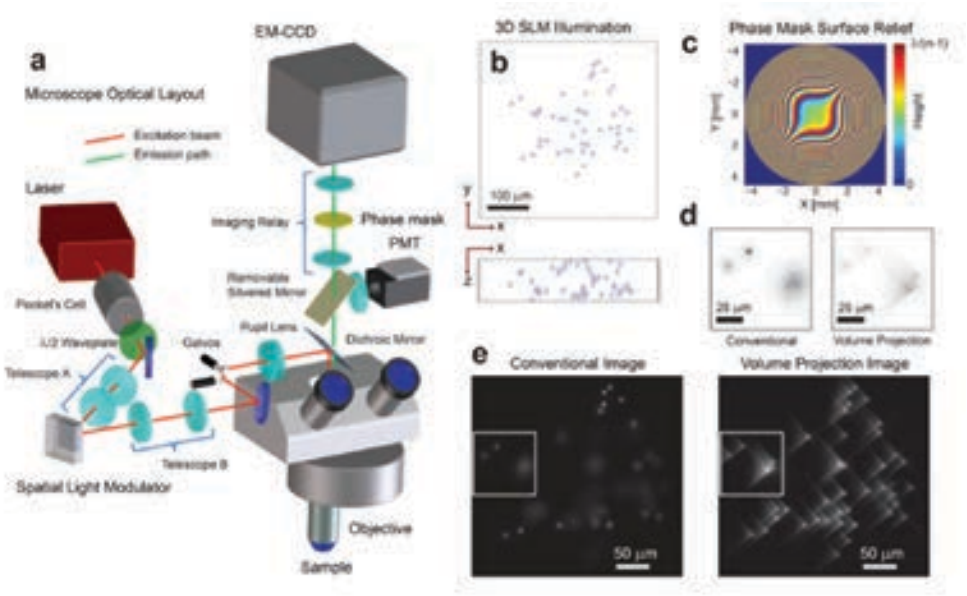

Figure 1. Optical path and characteristics of 3D projection-based imaging. ***A,*** The optical configuration comprises an illumination path which incorporates an SLM for 3D illumination and a modified imaging path using a phase mask to suppress the imaging effect of defocus. PMT, photomultiplier tube. ***B,*** An example 3D illumination pattern using a 20×/0.5NA objective. Scale bar, 100 µm. ***C,*** Ideal surface profile modulation of the phase mask. ***D,*** Experimental imaging results using a transparent fluorescent slab show that the volume projection imaging path results in clearer separation of the target signals when compared with the conventional imaging path. Note that the contrast conserves the number of photons in each image. Scale bars, 25 µm. ***E,*** Widefield imaging results comparing the conventional and volume projection imaging techniques. Note that each image is normalized to the respective peak signal. Scale bars, 50 µm. Reprinted with permission from Quirin et al. (2014), their Fig. 1.

NOTES

an extended sample volume onto a two-dimensional (2D) image plane and is therefore optimized for high-speed, 3D data acquisition. We use a phase-only spatial light modulator (SLM) to create multiple well-defined beamlets of light that illuminate many neurons in parallel (Nikolenko et al., 2008), and then use a phase mask to simultaneous acquire their fluorescence with a camera (Fig. 1*a*) in what we call Volume Projection Imaging (Quirin et al., 2013). In this technique, cells are not restricted to a single plane and can be freely distributed throughout the 3D sample (Fig. 1*b*).

While SLM-based multisite excitation has been coupled to wide-field microscopy before, it has been limited to 2D acquisition (Nikolenko et al., 2008; Packer et al., 2012). Although in some samples (transparent, or effectively sparse) single-photon excitation is sufficient, we regard two-photon capabilities as essential in turbid environments and for allowing precise modulation of activity when coupled with optogenetics or caged compounds (Packer et al., 2012).

Operationally, in our method, structural volume data are first acquired with a conventional two-photon microscope in order to identify the cells to be used for SLM targeting. We then generate a hologram that targets the regions of interest (ROIs) in the volume (Quirin et al., 2013) and image the functional activity of these ROIs simultaneously in 3D using a wavefront coded imaging system (e.g., a cubic phase mask) (Dowski and Cathey, 1995; Cathey and Dowski, 2002; Quirin et al., 2013). The deterministic illumination the SLM provides imparts a priori knowledge that can be used to extract additional information from the collected image, as explained below.

For simultaneous 3D signal acquisition, the wavefront coded imaging system enhances the standard shallow depth-of-field while maintaining the full aperture of the objective. This custom imaging system uses a phase-only optical mask in the imaging path to effectively null-defocus (Dowski and Cathey, 1995). This has the effect of greatly reducing the axial dependence of the point spread function (PSF) (i.e., the image is invariant to the 3D target position) and records an aberrated line-of-sight projection of the sample volume onto the image plane. This phase mask is described by the complex amplitude profile,

$$p(x,y) = ei^{2\pi\alpha(x^3 + y^3)}, \quad (1)$$

where we used values of α = 17 and 12 for M = 20×/0.5NA and 40×/0.8NA objectives, respectively, and x and y are the normalized coordinates of the microscope pupil (Fig. 1*c*).

The trade-off for this defocus invariance is a decreased contrast in the focused image (Fig. 1*d*) (Cathey and Dowski, 2002; Quirin et al., 2013). As a result, the acquired wide-field image exhibits a characteristic blur (e.g., an aberrated Point Spread Function) that is now invariant regardless of the 3D location of the target (Fig. 1*e*). This blur is nonetheless spatially restricted, and reduction of the out-of-focus PSF size compared with traditional imaging allows for a much higher local spatial density of targeted ROIs (Fig. 1*d*). Now, 3D fluorescence signals can be simultaneously acquired without loss of contrast owing to out-of-focus collection (Fig. 1*e*). As an additional benefit, the data volume is projected onto a 2D image plane, thereby reducing the total data throughput required during acquisition. In principle, this image can be digitally restored to diffraction-limited resolution by use of deconvolution methods; however, these steps are not necessary here (Cathey and Dowski, 2002). Instead, we report results using simple functional signal extraction, as described in Materials and Methods.

Demonstration of the Imaging Technique in Animals

Mouse models

We first demonstrated the system capabilities using a calcium indicator in *in vitro* mouse hippocampus preparations. Sections of the dentate gyrus were selected for 3D imaging, because this brain structure, with its dense ensemble of cells, provides a challenging opportunity to demonstrate single-cell resolution (Fig. 2*a*). Recent work has demonstrated the presence and importance of functional cell-cluster activity in 2D imaging conditions of the hippocampus (Muldoon et al., 2013; Ramirez et al., 2013); however, these events have never been observed in 3D. We present here a representative result of the 3D structure, which was first acquired and then used to identify the targets (Fig. 2*a*). We subsequently targeted all visually identified cells with illumination beamlets by loading the associated hologram pattern on the SLM (Quirin et al., 2013).

In one demonstration, data were acquired for 107 such targets and recorded using an EM-CCD detector at 55 volume projection images per second (VPPS) (Fig. 2*b*). Individual fluorescence activity from a dense 3D cluster of cells demonstrated that unique signals from individual neurons can be extracted with high signal-to-noise ratio (SNR). Before and after one identified burst, independent activity was observed in each cell body regardless of 3D position, demonstrating cellular resolution. A key advantage of this method is that minute differences in the onset

timing and calcium dynamics can be resolved with high SNR, even at these high temporal sampling rates (Fig. 2C). In slices from older animals, with less dense labeling, we demonstrated this method at sampling rates up to 125 VPPS at single-cell resolution and with high SNR. Cofiring dentate gyrus cells could represent ensembles of hippocampus neurons involved in pattern separation (Muldoon et al., 2013; Ramirez et al., 2013). Our technique thus allows for the visualization of these memory patterns with unprecedented spatiotemporal precision.

Larval zebrafish

We also report on the reconstruction of neuronal activity of the larval zebrafish (P7) with GCaMP5G (Akerboom et al., 2012; Ahrens et al., 2013) to map the temporal record of brainwide calcium transients at high speed *in vivo*. Different spatial scales can be accessed with our optical technique by simply selecting an alternative microscope objective or modulating the phase aberration present on the wavefront coding element at the pupil (via use of α, in Eq. 1). As a reference illustration, we show conventional two-photon galvanometric scanning images that contain brainwide activity patterns in which both individual cells and neuropil are recruited and fluoresce (Figs. 3*a*, *e*) (Ahrens et al., 2013). In recent work, the temporal resolution of such whole-brain activity mapping has been limited by the axial scan speed and the camera frame rate. In contrast, the technique proposed here has no moving parts, and therefore exhibits no mechanical acquisition speed limitation, nor the potential of coupling motion into the sample.

As a test case, 49 total target locations within a 350 × 350 × 150 μm volume were selected. Using these targets, a custom hologram was created and loaded to the SLM (red targets, Fig. 3*b*). With the two-photon SLM illumination, multiple waves of calcium transients were precisely localized as they occurred at 30 VPPS. The monitored active cells in these waves were temporally sorted based on the activity in the first wave, and we observed that this ordering was preserved in subsequent waves, with subsecond precision, despite occurring many minutes later (Fig. 3*c*). Within the monitored cells, the spatial distribution of the activity was dispersed throughout the sample, with varying modulation strength (Fig. 3*d*). This is the first demonstration of simultaneous 3D calcium activity imaging in *in vivo* zebrafish preparations with single-cell precision at a temporal resolution sufficient to resolve the dynamics of synaptic activity patterns.

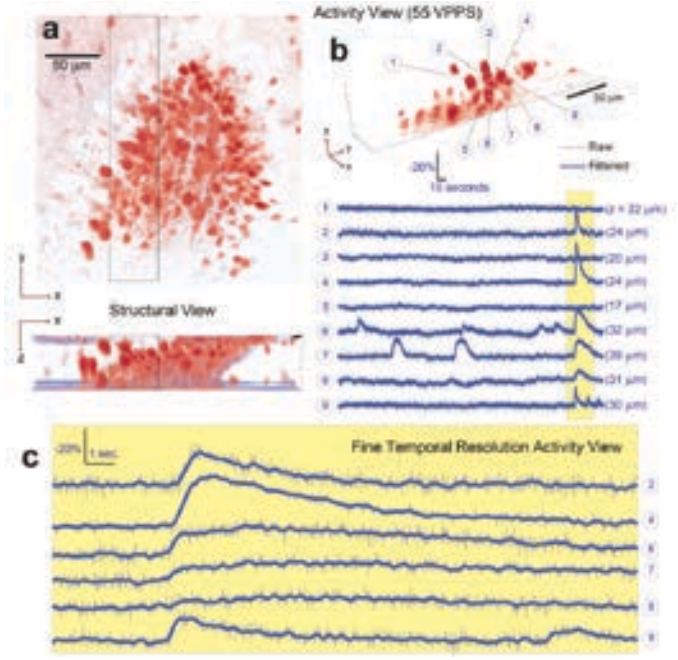

Figure 2. Simultaneous 3D imaging of hippocampal neuronal activity *in vitro* at 55 VPPS. ***A,*** 3D structural data acquired by two-photon scanning image stack. ***B,*** 3D imaging capability with single-cell resolution is demonstrated, where 9 of 107 total cells are selected from the 3D volume (boxed region in ***A***) and their respective activity is given in ***B.*** Despite simultaneous burst activity in 5 of the neighboring cells, independent calcium transients were measured. The axial location of each cell is given in parenthesis behind the respective fluorescence trace. ***C,*** A fine-temporal resolution view of the burst activity highlights the variability in both the temporal and amplitude modulation of the calcium transients. Reprinted with permission from Quirin et al. (2014), their Fig. 3.

Although the larval zebrafish is transparent, many organisms are not. Our method, as implemented here, still relies on direct imaging and is adversely affected in highly scattering environments. This has been a challenge for all imaging methods in neuroscience, and the described method is not immune to it. We evaluated the effect of scattering on the PSF used here and believe that this method can be applied up to 2–3 scattering lengths deep, provided that a sparse selection of 3D points is used. However, with the active development of red-shifted indicators and light sources whose longer wavelengths penetrate more deeply through tissue, this method may allow for significant and sizable volumetric imaging with high spatial and temporal resolution. Additionally, with the development of faster SLMs, or additional modulation schemes, temporal multiplexing can be added to augment the selectivity at large imaging depths (Ducros et al., 2013). This could be a critical

NOTES

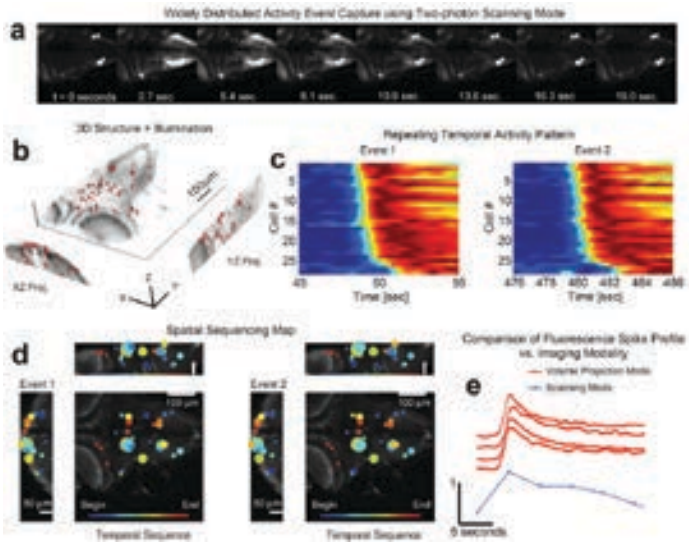

Figure 3. Simultaneous 3D imaging of calcium dynamics of zebrafish *in vivo* at 30 VPPS. ***a,*** Conventional single plane two-photon data acquisition reveals sequences of coordinated whole-brain activity. ***b,*** 49 targets are distributed throughout an acquisition volume of 284 × 270 × 114 µm to sample activity in 3D. Scale bar, 100 µm. ***c,*** Multiple repetitions of these events occur and exhibit similar time courses. ***d,*** The associated spatial patterns of the events confirm that the activity has repetitive structure. The size of the marker indicates the amplitude of signal modulation at each location. ***e,*** Comparison of the fluorescence spike time profile between the two imaging modalities shows the signal of the volume projection technique to be consistent with the two-photon scanning acquisition. The scanning mode data series was taken from the boxed area in ***a***, while the four-volume projection mode series was taken from the *x*-marked areas. Note that the fluorescence signal has been normalized in each time series of ***c*** and ***e*** for visualization. Reprinted with permission from Quirin et al. (2014), their Fig. 7.

improvement, since it would allow for imaging neurons whose projections fall within the same pixels of the camera.

Materials and Methods

Animals

All animal experiments were performed in accordance with the regulations and guidelines of Columbia University and were approved by the institutional review board of Columbia University. Mice experiments were performed in C57BL mice aged P11–P60 using 400-µm-thick coronal slices loaded with FURA-2AM. Zebrafish experiments were performed at ages P6–P8 and were performed in accordance with the regulations and guidelines of Columbia University. The zebrafish sample is held fixed within a bead of 2% low-melting point agarose to reduce motion artifacts.

Setup

The structured-illumination microscope with volume projection imaging uses one laser line for exciting fluorescence of either the calcium indicator dye or genetically encoded calcium indicator (GECI). This laser line is output from a Coherent Mira-HP (~140 fs pulses, 80 MHz) (Coherent, Santa Clara, CA), which can be manually tuned to span an excitation wavelength from 770 nm to 1100 nm. At λ = 800 nm, the system provides 3.8 W, and at λ = 920 nm, it provides 2.2 W. The output beam was steered through an electro-optic (EO) modulation device (ConOptics EO350-160, ConOptics, Danbury, CT). A broadband $\lambda/2$ wave plate (Thorlabs AHWP05M-980, Thorlabs, Newton, NJ) was located after the EO modulator to rotate the polarization state to be parallel with the active axis of the SLM (XY-512 Spatial Light Modulator, Boulder Nonlinear Systems, Lafayette, CO) located downstream. An LS6Z2 shutter (Vincent Associates, Rochester, NY) was placed in the beam path in order to control illumination conditions. A 1:2 telescope (f_1 = 50 mm, f_2 = 100 mm; Thorlabs plano-convex lenses) scaled the optical beam to approximately fill the active area of the SLM (XY-512, Boulder Nonlinear Systems). The optical beam was redirected by a periscope to illuminate the SLM. The SLM has a custom lookup table that was experimentally determined at both wavelengths reported for use. The angle of incidence of the illumination beam to the SLM was ~10°. A 4:1 telescope (f_3 = 300 mm, f_4 = 75 mm; Thorlabs plano-convex lenses) reduces the image of the SLM onto a set of galvanometer mirrors. The galvanometer mirrors are located conjugate to the microscope objective pupil of an Olympus BX51 microscope (Olympus America, Melville, NY) by use of an Olympus pupil transfer lens (f_5 = 50 mm) and the mounted tube lens (f_{TL} = 180 mm).

Two microscope objectives were tested in the manuscript: an Olympus 20×/0.5NA WI and an Olympus 40×/0.8NA WI objective. To operate in a two-photon scanning mode, Olympus Fluoview was used to control the galvos and image acquisition from a photomultiplier tube (PMT) (H7422P-40, Hamamatsu) located above the microscope. A removable silvered mirror (mounted in Thorlabs LC6W and LB4C) redirects the collected fluorescence emission into the PMT module. To operate in volume projection mode, custom software was developed for MATLAB (MathWorks, Natick, MA) to load the correct gamma map and generate a hologram with manually selected targets throughout the sample volume. When the illumination shutter is opened, the sample is illuminated with a custom pattern that is representative of where the targeted cell soma are located. For volume projection image acquisition, the silvered redirection mirror for the PMT is removed, and the fluorescence emission is passed through an optical relay system with a custom phase mask. The optical relay consists of a 1:1 telescope (f_{4f} = 150 mm, Thorlabs 2" achromatic doublets) with a custom-designed surface relief patterned onto a 1" diameter quartz plate, which is placed a distance f_{4f} behind the first lens. Note that no amplitude modulation is necessary (i.e., the mask is transparent), which is critical for high-sensitivity imaging. Also note that in the following, the imaginary component describes the surface relief of the mask where

$$h(x,y) = \left(\frac{arg\,[p(x,y)]}{2\pi}\right)\left(\frac{\lambda}{n-1}\right) \quad (2)$$

and where h is the height, $p(x,y)$ is the complex function describing the pupil, λ is the emission wavelength, and n is the refractive index of the substrate (here, we used fused quartz with n = 1.462 at λ = 515 nm). The realized surface relief is representative of a discretized 8-level diffractive optic design of this profile with α = 200 over an 18 mm diameter and with an optimal $\lambda \approx$ 505 nm. An imaging detector (Andor iXon Ultra 897 electron-multiplying [EM] CCD, Andor Technology, Belfast, UK) is located in the imaging plane of the 1:1 relay system.

Targeting calibration, image acquisition, and signal reconstruction

Precise targeting of the neuron cells was facilitated by a 3D calibration of the SLM projection patterns. A calibration phantom was created using a 2% agarose mixture with a dye solution (yellow highlighter dye) at a 1:1 ratio. Standard projection patterns were input to the SLM, and the captured fluorescence image was used at each z position to calculate an affine transformation from the SLM to the EM-CCD. A third-order polynomial fit of each element from the axial-dependent affine matrix describing the axial evolution of the affine transform matrix was made and stored for later use. A pollen grain slide was used to calibrate the axial-dependent affine transformation from the EM-CCD image to the PMT image frame. The slide was translated through the volume range of interest, and an EM-CCD image and PMT image were acquired for comparison. An automated fitting routing estimated the axial-dependent affine transform matrix and, as was performed with the SLM to EM-CCD transform, a third-order polynomial fit was made to each element of the matrix. Matrix multiplication of the PMT to EM-CCD and the EM-CCD to SLM transforms yielded the coordinates to load onto the SLM for precise targeting.

Images acquired in volume projection mode on the imaging detector were processed using custom analysis software written in MATLAB (MathWorks, Natick, MA). Volume projection acquisition mode consists of generating the hologram illumination pattern, setting the EO modulator for appropriate illumination power, opening the shutter, and acquiring time-lapse images, which were stored as TIFs (image acquisition used an Andor Solis environment, Andor Technology). Because the neurons were relatively large compared with the imaging detector pixel size, pixel binning of 4 × 4 was routinely used to improve SNR without any appreciable loss of spatial resolution performance. Using the targeting calibration matrices, the location of each target on the CCD was estimated and an experimentally measured PSF put in its place in order to form a basis set of images: one image for each target. Each frame from the time-lapse stack of images was decomposed into a linear superposition of this basis set using a least-squares fitting, plus one image for background estimation. Formally, this was accomplished by creating a matrix of N images,

$$\mathsf{B} = \begin{bmatrix} (B_i(1) & \cdots & B_N(1) \\ \cdots & \cdots & \cdots \\ B_i(m*n) & \cdots & B_N(m*n) \end{bmatrix} \quad (3)$$

where each column is one $m \times n$ image, lexicographically ordered in a column, representative of the expected pattern from the target location (known from the deterministic illumination). In principle, these images can be given by simulation or found experimentally. Here, we used the experimentally determined PSF and built the library by stamping it at each target location. Given acquisition of the experimental image, $\mathsf{I}(t)$, at time t and using

NOTES

$$I(t) = B \cdot W(t) + n \quad (4)$$

to describe the image formation, where n is additive random noise, a least-squares fitting

$$\hat{W}(t) = \min_{W(t)} \|I(t) - B \cdot W(t)\|^2 \quad (5)$$

quickly yields the individual fluorescence from each target, $w_i(t)$.

To control for systematic movements of the sample that could have been artificially interpreted as calcium transients, we ruled out the possibility of synchronous deflections in fluorescent transients in either direction. We also performed a positive movement test by gently tapping the sample stage, which resulted in the characteristic synchronous fluorescence signals.

Conclusion

In conclusion, we have presented a technique for fast, simultaneous, two-photon optical data acquisition of neuron activity that is distributed throughout three dimensions. This has been demonstrated in multiple animal preparations, both *in vitro* and *in vivo*, that are relevant for neuroscience. Both the illumination and data acquisition are simultaneous and can target multiple ROIs throughout the volume of tissue, allowing for parallel activation and imaging. Advances in lasers and SLMs may enable more complex patterns, and faster cameras could accommodate direct imaging of voltage activity in 3D. Also, although we describe two-photon SLM-based multiple beamlet excitation here, any predetermined structured illumination could be used.

The combination of holographic illumination with volume projection imaging appears to us an ideal platform for future work on brain activity mapping.

Acknowledgments

We thank Misha Ahrens and David Bennett for their help with the fish preparations and their comments on the manuscript. This work was supported by the National Eye Institute (DP1EY024503, R01EY011787), National Institute of Mental Health (R01MH101218), Defense Advanced Research Projects Agency (DARPA) contract W91NF-14-1-0269, and the Keck Foundation. This material is based on work supported by, or in part by, the U.S. Army Research Laboratory and the U.S. Army Research Office under contract number W911NF-12-1-0594 (Multidisciplinary University Research Initiative).

S. Q. and D. S. P. designed and built the microscope software and hardware. S.Q., J. J., D. S. P., R. Y. designed the mouse experiments. S. Q., and R. Y. designed the zebrafish experiments. S. Q. and J. J. performed the mouse experiments and analyzed data. S. Q. performed the zebrafish experiments. S. Q., D. S. P. and R. Y. wrote the paper. Parts of this chapter have been previously published in Quirin et al. (2014), Simultaneous imaging of neural activity in three dimensions, Front Neural Circuits 8:29.

References

Ahrens MB, Orger MB, Robson DN, Li JM, Keller PJ (2013) Whole-brain functional imaging at cellular resolution using light-sheet microscopy. Nat Methods 10, 413–420.

Akerboom J, Chen TW, Wardill TJ, Tian L, Marvin JS, Mutlu S, Calderon NC, Esposti F, Borghuis BG, Sun XR, Gordus A, Orger MB, Portugues R, Engert F, Macklin JJ, Filosa A, Aggarwal A, Kerr RA, Takagi R, Kracun S, et al. (2012) Optimization of a GCaMP calcium indicator for neural activity imaging. J Neurosci 32:13819–13840.

Alivisatos AP, Chun M, Church GM, Greenspan RJ, Roukes ML, Yuste R (2012) The brain activity map project and the challenge of functional connectomics. Neuron 74:970–974.

Cathey WT, Dowski ER (2002) New paradigm for imaging systems. Appl Opt 41:6080–6092.

Chen TW, Wardill TJ, Sun Y, Pulver SR, Renninger SL, Baohan A, Schreiter ER, Kerr RA, Orger MB, Jayaraman V, Looger LL, Svoboda K, Kim DS (2013) Ultrasensitive fluorescent proteins for imaging neuronal activity. Nature 499:295–300.

Cheng A, Goncalves JT, Golshani P, Arisaka K, Portera-Cailliau C (2011) Simultaneous two-photon calcium imaging at different depths with spatiotemporal multiplexing. Nat Methods 8:139–142.

Dowski ER, Cathey WT (1995) Extended depth of field through wave-front coding. Appl Opt 34:1859–1866.

Ducros M, Houssen YG, Bradley J, de Sars V, Charpak S (2013) Encoded multisite two-photon microscopy. Proc Natl Acad Sci USA 110:13138–13143.

Gobel W, Kampa BM, Helmchen F (2007) Imaging cellular network dynamics in three dimensions using fast 3D laser scanning. Nat Methods 4:73–79.

Horton NG, Wang K, Kobat D, Clark C, Wise F, Schaffer C, Xu C (2013) *In vivo* three-photon microscopy of subcortical structures of an intact mouse brain. Nat Photonics 7:205–209.

Katona G, Szalay G, Maak P, Kaszas A, Veress M, Hillier D, Chiovini B, Vizi ES, Roska B, Rózsa B (2012) Fast two-photon *in vivo* imaging with three-dimensional random-access scanning in large tissue volumes. Nat Methods 9:201–208.

Kralj J, Douglass AD, Hochbaum DR, Maclaurin D, Cohen AE (2012) Optical recording of action potentials in mammalian neurons using a microbial rhodopsin. Nat Methods 9:90–95.

Muldoon SF, Soltesz I, Cossart R (2013) Spatially clustered neuronal assemblies comprise the microstructure of synchrony in chronically epileptic networks. Proc Natl Acad Sci USA 110:3567–3572.

Nikolenko V, Watson BO, Araya R, Woodruff A, Peterka DS, Yuste R (2008) SLM microscopy: scanless two-photon imaging and photostimulation with spatial light modulators. Front Neural Circuits 2:1–14.

Packer AM, Peterka DS, Hirtz JJ, Prakash R, Deisseroth K, Yuste R (2012) Two-photon optogenetics of dendritic spines and neural circuits. Nat Methods 9:1202–1205.

Quirin S, Peterka DS, Yuste R (2013) Instantaneous three-dimensional sensing using spatial light modulator illumination with extended depth of field imaging. Opt Express 21:16007–16021.

Quirin S, Jackson J, Peterka DS, Yuste R (2014) Simultaneous imaging of neural activity in three dimensions. Front Neural Circuits 8:29.

Ramirez S, Liu X, Lin P-A, Suh J, Pignatelli M, Redondo RL, Ryan TJ, Tonegawa S (2013) Creating a false memory in the hippocampus. Science 341:387–391.

Yuste R, Katz LC (1991) Control of postsynaptic Ca^{2+} influx in developing neocortex by excitatory and inhibitory neurotransmitters. Neuron 6:333–344.